Metals & corrosion

A crystallographic study of the deformation mechanisms during small punch testing of 14wt%Cr oxide dispersion steel

S. Samuha[1,*] (iD), Y. Templeman[2], S. Haroush[1], G. M. Guttmann[1], M. Pinkas[1], and L. Meshi[2]

[1] *Nuclear Research Center-Negev, P.O. Box 9001, 84190 Beer-Sheva, Israel*
[2] *Department of Materials Engineering, Ben-Gurion University of the Negev, 84015 Beer Sheva, Israel*

ABSTRACT

With their excellent resistance to high-temperature creep and irradiation swelling, the oxide dispersion strengthened (ODS) ferritic steels are considered promising structural materials for future reactors. The characteristic anisotropy of these materials, imposed by their fabrication processes, is considered both beneficial and harmful, depending on the specific application. Current research has addressed the effect of anisotropy on mechanical properties by analyzing deformation mechanisms operating during the small punch testing (SPT). As a case study, 14wt%Cr ODS steel rod was studied before and post SPT along and perpendicular to the extrusion direction. In order to assess the effect of the anisotropy, this study incorporates extensive microstructural characterization alongside quantitative textural analysis. Nucleation of cracks and their subsequent propagation are discussed, taking grain boundary characteristics, grain morphology, texture, and the effect of dispersed particles into account.

Introduction

Designs of future power plants, referred to as Generation IV, are driven by the desire to increase the operating temperature up to 650 °C as compared to 350 °C in pressurized water reactors. The Oxide Dispersion Strengthened (ODS) ferritic steel has a great potential to be used as the fuel cladding material in such reactors [1, 2] due to its superior creep resistance at high temperature and good resistance to corrosion and swelling [3–5].

ODS alloys are typically fabricated by powder metallurgy and consolidation processes resulting in pronounced microstructural inhomogeneities, responsible for unique and anisotropic mechanical properties of the deformed materials. As stated above, these properties make ODS ferritic steels suitable candidates to serve as fuel cladding since this

---

Handling Editor: N. Ravishankar.

Address correspondence to E-mail: samuha@post.bgu.ac.il

🖄 Springer

application requires enhanced creep resistance in the hoop direction. The anisotropy of mechanical properties is related to (1) morphology, reflected in the bimodal grain size distribution of fine grains laced along elongated grains with a high grain aspect ratio [6], (2) crystallographic texture formation with < 110 > preferred orientation along a reference direction [7], (3) distinct spread/dispersion and size of the oxides, carbides and/or nitrides [8, 9]. Variation in one of mentioned above parameters dramatically affects the mechanical properties of the ODS steels [10]. Furthermore, post-processing heat treatments and plastic forming can alter the degree of anisotropy of mechanical properties [11, 12].

Another property of ferritic ODS steels, which is advantageous for the intended industrial application, is the enhanced corrosion resistance due to the relatively high Cr content. Nevertheless, high Cr content may lead to embitterment during exposure to high temperatures due to the separation to Fe-rich and Cr-rich phases [13–15]. Thus, this material has to be monitored concerning possible degradation of mechanical properties following service under the severe conditions of a nuclear reactor. The small punch test (SPT) method [16], which was developed to characterize the mechanical behavior of small or thin specimens, can be used for such monitoring. The SPT concept is based on locking a thin sheet-like specimen between two dies and pushing against it a spherical cap-punch up to failure. Unlike standard tension test, the stresses and strains developing in the specimen during the SPT test are not uniaxial. Therefore, the estimation of mechanical properties requires further analysis, which was formulated and proved in various studies. Despite this disadvantage, SPT provides a good assessment tool [17] and is becoming more common in the materials research community.

Over the years, both conventional mechanical testing such as tensile tests, creep, and toughness [18, 19] and the less traditional SPT method [20] were performed in order to evaluate the mechanical properties of ODS steels. Despite the extensive number of reports, only a few incorporated results of these tests with a thorough investigation of the microstructure and texture analysis [11]. As a result, a fundamental and solid understanding of the plasticity mechanisms and their relation to anisotropy is still lacking.

This paper aims to provide an insight on the key role of anisotropy on the deformation mechanisms of a Fe–14Cr ODS alloy during the SP test. In this case, SPT is the most suitable test method due to the dimensions of the extruded ODS rod, which prevent using conventional tension test perpendicular to the extrusion direction. To meet the stated goal, the research incorporates extensive electron microscopy characterization alongside quantitative textural analysis using various electron diffraction techniques.

Experimental procedure

Material

The 14wt%Cr ODS steel was received from CEA/DEN/DANS, France. The fabrication process included mechanical alloying (MA) of the raw powders, consolidation of the powders by hot extrusion in the form of bars at 1100 °C, hot isostatic pressure at 1050 °C, and 1400 bar for 4 h and finally annealing treatment at 1050 °C for 1 h. Initial characterization of the microstructure and full characterization of strengthening dispersoids were published in [21].

Mechanical properties

SP experiments were performed on the 8 × 8 × 0.5 mm samples using the same apparatus described in [22–24], with a 2.4 mm diameter hard steel ball at a stroke control. Square-shaped plates of 8 mm in length were cut by spark erosion from the as-extruded bar along two different orientations, as described in Fig. 1. The plates differentiate by the relative directions of the loading (LD), extrusion (ED) and normal (ND). The notations longitudinal ('L') and transverse ('T') refer to LD parallel and perpendicular to the ED, respectively. The plate-shaped specimens were subsequently ground on a SiC paper in the hierarchical sequence of 240, 400, 600, 800, 1200, and 4000 grit, down to a nominal thickness of 0.5 mm. The SP test was conducted in the following steps: (1) clamping of the specimen between the dies under 600 N, (2) pre-load up to 15 N and balance the stoke transducer (Instron, COD), (3) pushing the hemispherical punch head into the specimen under a stroke control at a speed of 0.1 mm/min, up to failure. SP test was performed on three samples for each direction (L and T). The load–displacement SPT
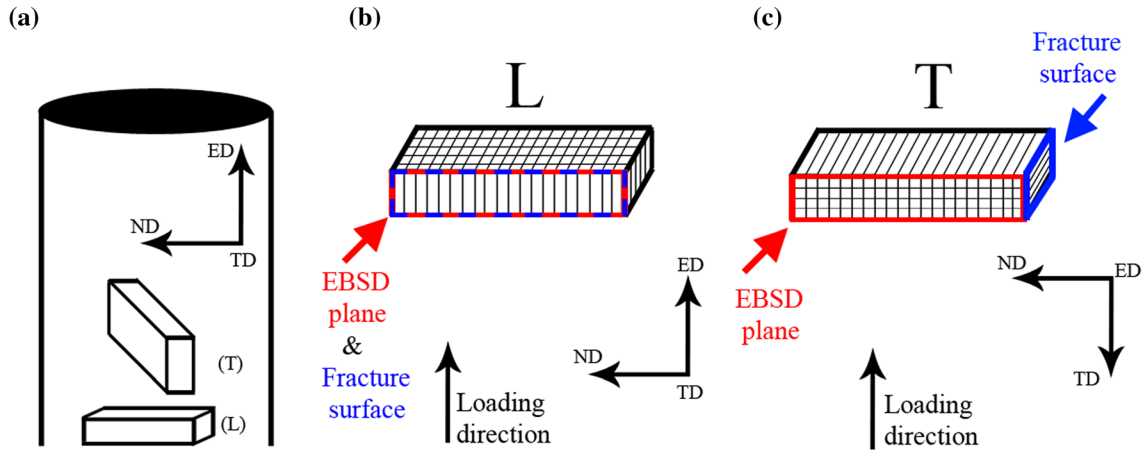
Figure 1 Schematic representation of the (**a**) extruded rod, (**b**) the longitudinal (*L*), and (**c**) the transverse (*T*) specimens. In (**b**) and (**c**) are detailed presentations of the *L* and *T*-SPT samples. The extrusion direction, loading direction, and specimen orientations (ED, LD, *L*, and *T*) are shown. In (**b**, **c**), rectangles represent the elongated grains along with the ED in the schematics. EBSD and fracture surfaces are marked by red and blue squares, respectively. For the interpretation of the colors, the reader is referred to the web version of this article.

curves were analyzed by the $P_{t/10}$ calculation method, previously reported by Garcia et al. [16], for obtaining the yield, $\sigma_{0.2}$, and ultimate tensile, σ_{UTS}, strength values.

Microstructural characterization and texture analysis

Microstructure, micro-texture, and fracture surfaces were characterized using field emission gun scanning electron microscope (FEG-SEM) coupled with Electron Back-Scattered Diffraction (EBSD) detector. Figure 2a, b display SEM images captured in low magnifications of the cross section of the *T* and the *L* samples, respectively, after the SPT test. Two uniquely designated regions were studied: (a) the heavily deformed zone, closest to a crack tip ('A' zone), and (b) at the grip representing the as-received state ('B' zone). In the *T*-oriented sample, two macro-cracks were noticed at different locations (namely, A_1 and A_2), each will be discussed separately.

During surface preparation for EBSD analysis, undesired bending of the curved samples was minimized by the following steps: (1) side mounting in Bakelite; (2) grinding and polishing on SiC papers from 600 to 4000 grit; (3) final polishing on diamond suspension from 5 to 0.5 μm grain sizes; (4) chemical–mechanical polishing using 0.05 μm colloidal silica for at least 4 h. At the end of these procedures, a plane surface with minor scratches was attained. As a result, sharp diffraction patterns were recorded and successfully interpreted based (solely) on the α-Fe phase. The EBSD acquisitions were carried out by scanning using a step size ranging from 0.2 to 0.025 μm, in accordance with the inspected Region of Interest (ROI), the severity of the local deformations, and the size of features at the relevant ROI. The ATEX package, a freely available toolbox, was employed for post-processing and visualization of the EBSD data [25]. Inverse pole figure (IPF) maps were used to characterize the microstructural evolution and texture modification. The grain-boundary
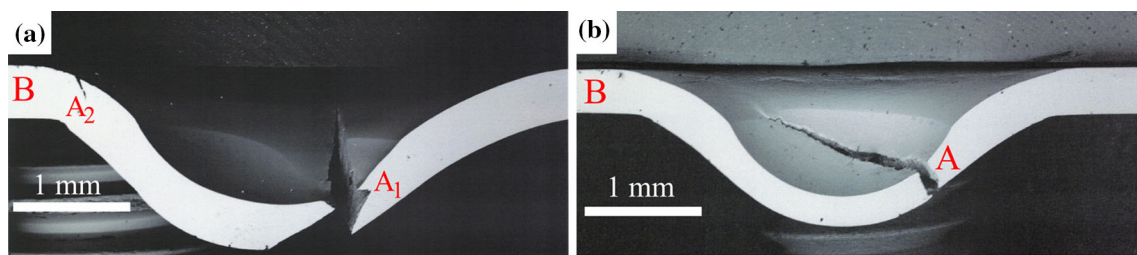

Figure 2 SEM image showing a cross-sectional surface of the **a** *T* and **b** *L* samples post SP test at near crack 'A' and grip 'B' regions.
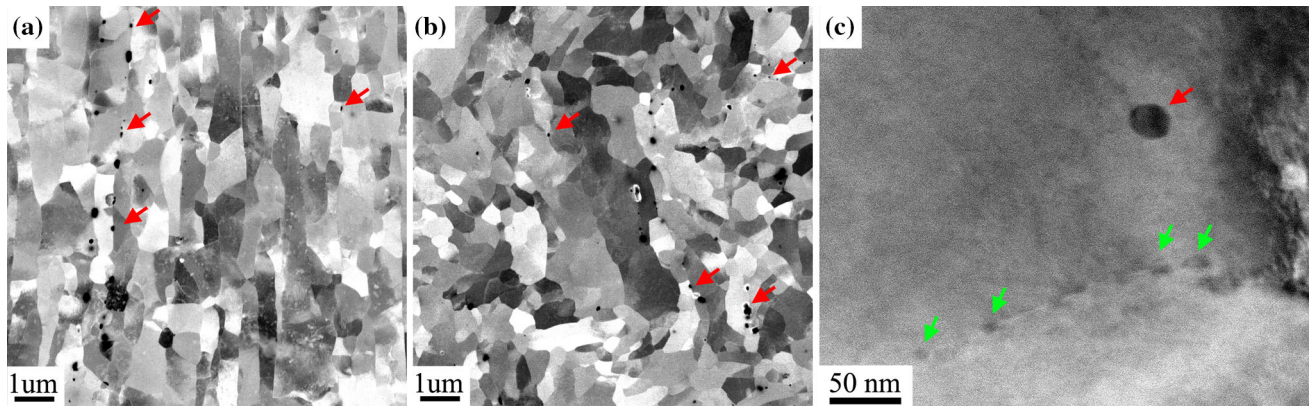
Figure 3 The two populations of particles observed in the 14wt%Cr ODS steel: **a–c** Ti–rich carbides and **c** nano-oxides. **a** and **b** are SEM images, in channeling contrast, for longitudinal and transverse orientations, respectively. **c** Bright Field (BF) TEM image of a Ti–rich carbide and nano-sized oxides along the grain boundaries. Red and green arrows point to the locations of the Ti–rich carbides and nano-sized oxides, respectively.
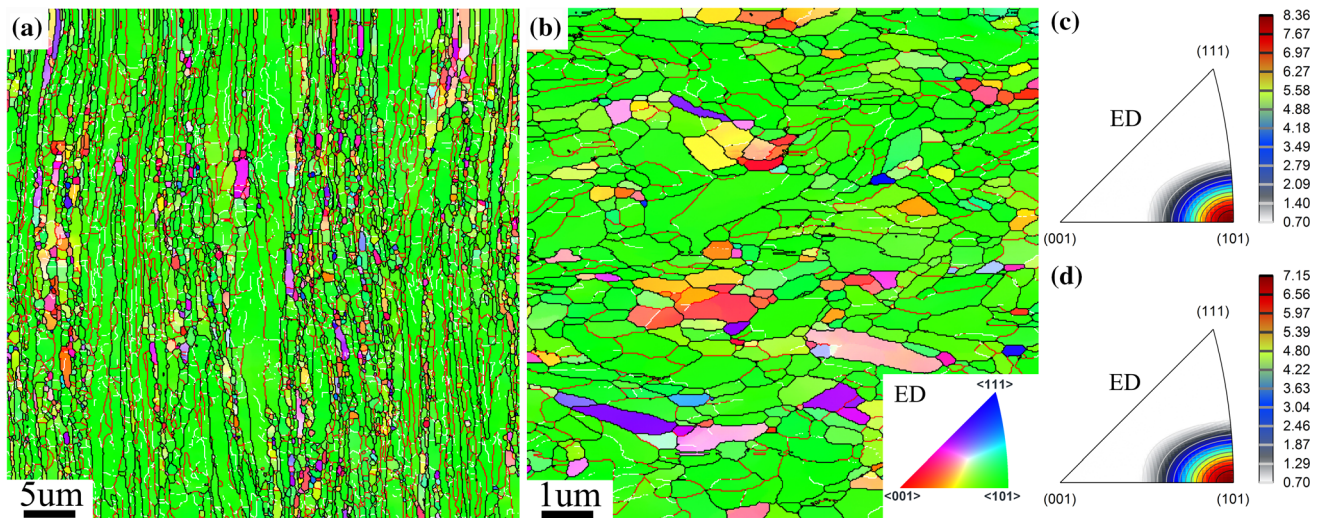

Figure 4 EBSD-IPF∥ED maps of the **a** longitudinal and **b** transverse samples. For illustration purpose, different magnification was used in the two cases. The orientation distribution in **c** and **d** was calculated based on images **a** and **b**, respectively. An inset color-coded key triangle indicates the crystallographic orientations. White, red, and black lines colors designate the LAGBs, MAGBs, and HAGBs, respectively. Multiple Random Distribution (MRD) values are located on the right side of each IPF. The reader is referred to the web version of this paper for the color representation of this figure.

distribution was categorized based on misorientation angle criteria [26]. Using these criteria, misorientation angles 2–5°, 5–15°, and 15–62.5° were categorized as low, medium, and high angle grain boundaries (LAGBs, MAGBs, and HAGBs), respectively. Microtexture analysis was performed through the computation of Orientation Distribution Functions (ODF), employing the harmonic expansion method, which assumes axial symmetry of an orthorhombic sample.

TEM investigation was carried out using a JEOL JEM-2100F TEM operating at 200 kV equipped with Jeol JED-2300 T EDS, scanning coils, and Gatan high angle annular dark-field (HAADF) detector.

Results

Microstructural investigation of the as-received samples

As mentioned, the as-received state was characterized along the SPT sample grip (marked as 'B' zone on Fig. 2). The fabrication route of the investigated
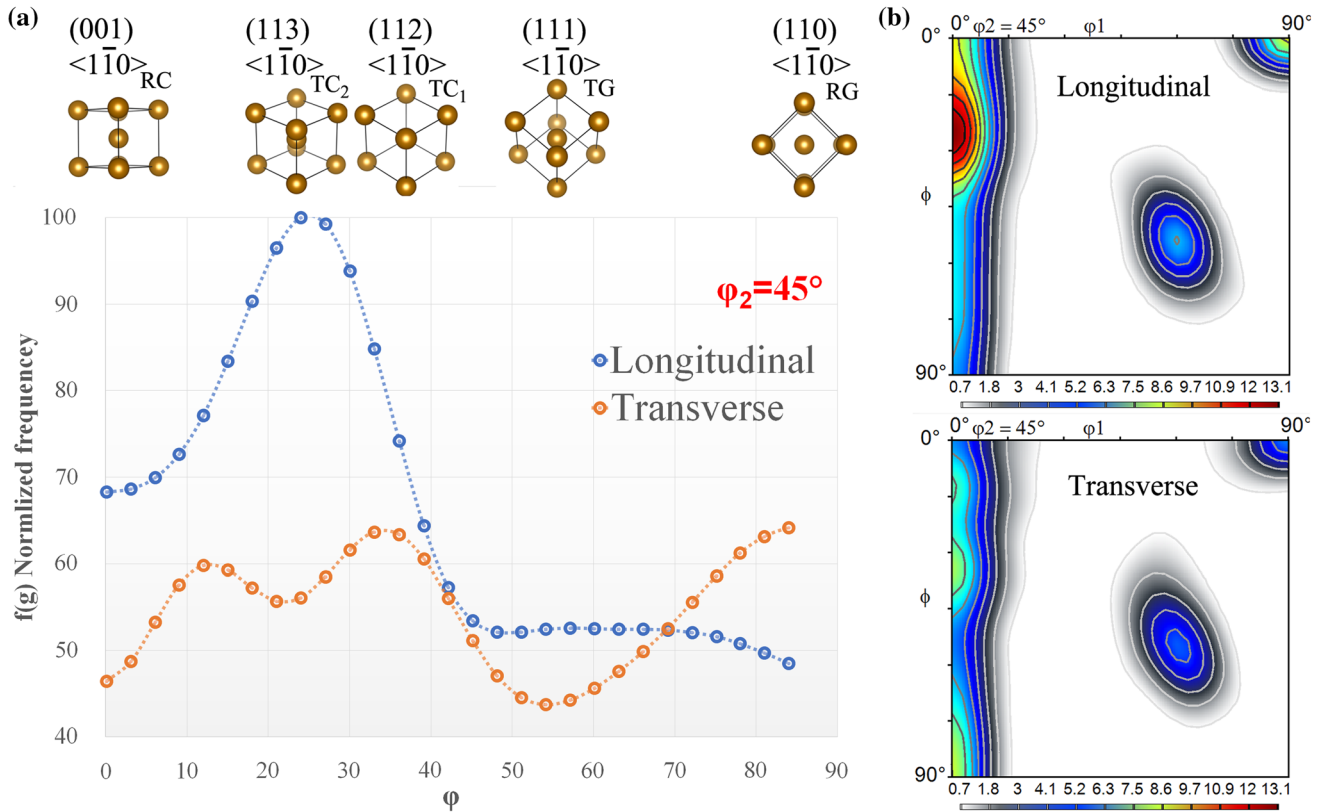
Figure 5 a Characteristic texture changes along the α-fiber and **b** ODF section at $\varphi_2 = 45°$. In **a**, the positions of main ideal orientations are presented alongside a schematic illustration of texture components. The reader is referred to the web version of this paper for the color representation of this figure.

Figure 6 Force–displacement curves obtained for three specimens taken at **a** longitudinal and **b** transverse orientations. The thickness of the samples in mm is given for each curve at (**a**) and (**b**).
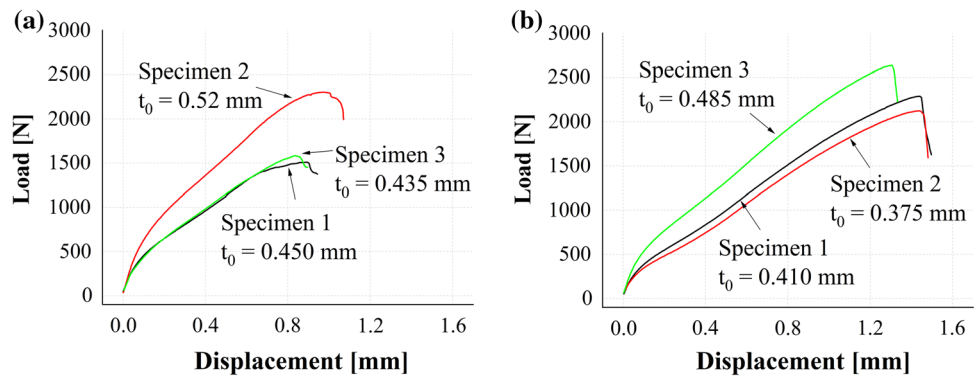

Table 1 Mechanical properties evaluated by tensile and SP tests

Sample	σ_y [MPa]	σ_{UTS} [MPa]	Elongation or deflection [%]
Tensile 'L' oriented	1079 ± 18	1180 ± 24	8.8 ± 0.14
SPT 'L' oriented	1027.5 ± 30.3	1108 ± 40	20.26 ± 3.5
SPT 'T' oriented	1085.5 ± 99.6	1162 ± 109	11.6 ± 0.3

14wt%Cr ODS steel imposed an inhomogeneous microstructure of the α-Fe (ferritic) matrix. A bimodal grain size distribution was noted for the longitudinally oriented specimen with elongated grains and densely packed colonies of semi-equiaxed fine grains, both arranged along with the ED

(Fig. 3a). While, in the transverse sample, the microstructure mainly consisted of small-sized and distorted grains (Fig. 3b).

Both orientations contained particles dispersed in the matrix, preferably located at the grain boundaries along with the ED. Such morphology is a result of the consolidation and extrusion processes. These particles can be classified into two main populations, distinguished by their characteristic dimensions, as shown in Fig. 3. The population, with sizes in the range of 50–200 nm, was identified as Ti-rich carbides (Fig. 3a–c) following EDS analysis, as described in previous work [21]. The population consisting of densely distributed nano-sized oxide particles, varying from several to 10 nm in size (Fig. 3c), was identified as oxides, preferably observed along the grain boundaries [21].

Textural analysis of the as-received samples

Figure 4a, b displays orientation maps parallel to the ED (i.e., EBSD-IPF||ED) for the longitudinal and transverse specimens, respectively. The orientations distribution in Fig. 4c, d are calculated from the images in Fig. 4a, b, respectively. Both samples exhibit strong preferential < 110 > texture direction, parallel to the ED, as derived from the high Multiple Random Distribution (MRD) values. Some grains with a relatively high angular deviation from the specified texture were detected in both directions, preferably small-sized grains in the longitudinal sample.

The α-fiber texture was quantitatively characterized using the orientation distribution function (ODF). In Fig. 5, the $\varphi_2 = 45°$ section (in Bunge notation), extracted from the Euler space, is presented for the longitudinal and transverse orientations. The characteristic textural changes are readily
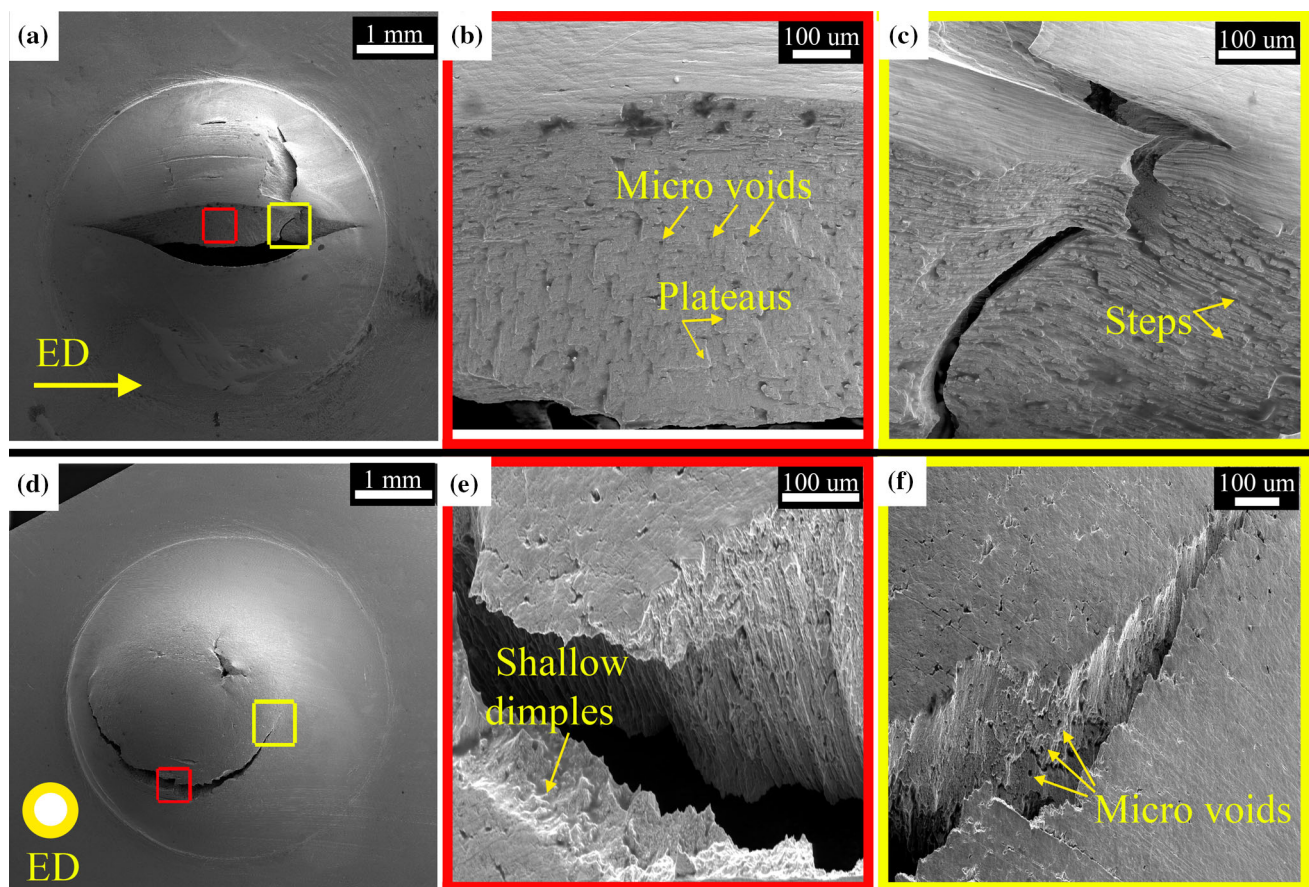

Figure 7 Fracture surface of **a–c** the transverse and **d–f** the longitudinal specimens. (**b**, **c**) and (**d**, **f**) are enlarged areas, marked by red and yellow squares at (**a**) and (**d**), respectively. Arrows point to fracture features of steps, dimples, and plateaus. ED marks the direction of extrusion. For the interpretation of the colors, the reader is referred to the web version of this article.

visualized by plotting the orientation density along the α-fiber (Fig. 5a). The texture components are represented as (hkl) $< uvw >$, which symbolize that {hkl} planes of the grains are parallel to the Normal Direction (ND) of the sample and that the $< uvw >$ direction of those grains is oriented parallel to the ED. The texture of an α-fiber with $< 110 >||$ED is analyzed according to five distinct orientations (Fig. 5): Rotate Cube (RC) $(100)[1\bar{1}0]$, Transformed Cupper (TC) 2 and 1, which are the $(113)[1\bar{1}0]$ and the $(112)[1\bar{1}0]$ orientations, Transformed Goss (TG), and the Rotated Goss (RG) texture components with the $(111)[1\bar{1}0]$ and the $(110)[1\bar{1}0]$ orientations, respectively. For clarity, orientations distribution is normalized by the $f(g)_{max}$. A schematic representation of these orientations is given in Fig. 5.

Notable differences in micro-texture between the longitudinal and the transverse specimens were observed. The extent of texture is greater in the longitudinal orientation, as manifested by the high intensities around the TC_2 $(f(g)_{max.})$ and RC $(0.7f(g)_{max.})$ components. In the transverse sample, some increase in the frequency of orientations close to TC_1, TC_2, and RG texture components is noticed.

SPT results

Figure 6 presents the measured load–displacement curves of SP tests. A total of three samples were tested for each orientation. The thickness of the samples is given for each curve. The calculated mechanical properties for the L and T samples in SP tests are given in Table 1. The standard tensile test validated the accuracy of the SP test, and the results are also presented in Table 1. It should be noted that tensile specimens were extracted only from the longitudinal orientation due to material limitations. The tensile specimens were standard according to ASTM E 8 m. The tests were conducted on stroke control at a rate of 0.2 mm/min. The tensile tests were repeated three times to ensure the accuracy of mechanical data. The differences between SPT and conventional tension results were less than 10%, which is within the acceptable measurement error.

The mechanical properties obtained in SP tests (Table 1) reveal elements of anisotropy. While yield and ultimate stresses in the longitudinal and transverse orientations were found to be almost identical, the deflection at F_{max} in the longitudinal (δ_{max}) is almost doubled as compared to the transverse orientation (1.4 mm vs. 0.8 mm).

SPT measurements of all samples resulted in a typical pattern containing four deformation regimes: zone (I) linear regime, which results from the elastic bending; zone (II) initial parabolic zone, representing plastic bending; zone (III) the semi-linear zone, representing the membrane stretching region, and zone (IV) which is the failure regime were plastic instability and cracking occurs. While similarities are noticed between zones II + III for all specimens, there are subtle differences in zone IV (see Fig. 6). The load drop following failure in the longitudinal direction is arrested and then resumes at an accelerating rate. Conversely, in the transverse direction following failure, an abrupt load drop is noticed.

Fracture surface analysis of samples post SPT

Figure 7a, d shows a general top-view of the fracture following SPT in the transverse and longitudinal orientations, respectively. Figure 7b, c and Fig. 7e, f present high magnification of specific regions, emphasized by red and yellow rectangles on Fig. 7a, d, respectively.

The T and L samples failed quite differently, with significant to subtle differences in the fracture mode and crack path. Both orientations showed crack deflection path in the form of a 'zig-zag.' In the T specimen (Fig. 7a), two macroscopic cracks were noticed in the A_1 region (marked in Fig. 2). The dominant crack crossed the center of the specimen along the ED. The secondary crack initiated at about a quarter of the indent and progressed perpendicular to the main crack. In the LD-ED plane, the crack traveled for some distance along approximately 45° line with respect to the loading axis before aligning with the LD, and, then, progressed once more along another 45° line with respect to LD (see Fig. 7d). The fracture surface is characteristic of cleavage with reasonably smooth plateaus (cleavage facets) throughout the specimen thickness. At higher magnifications, the lack of dimples confirmed brittle fracture mode, prevailing for this orientation.

On the other hand, the L sample fails in a ductile manner, as indicated by the circumferential crack along the contact between the punch and the specimen (Fig. 7d). The fracture surface featured shallow dimples and fine microvoids, supporting the ductile
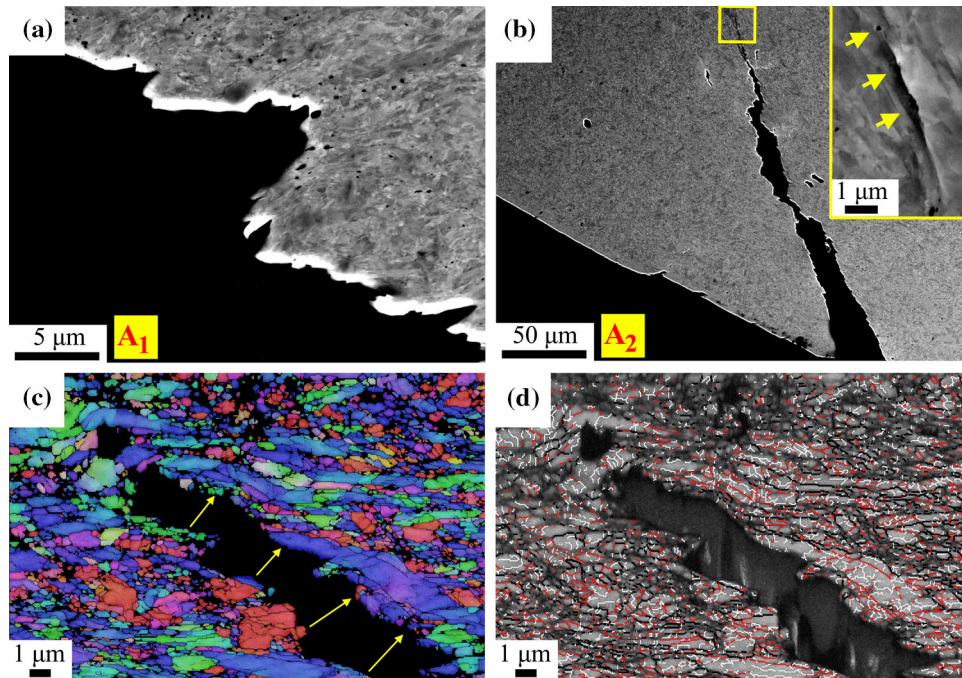
Figure 8 Cross-section view of the fracture surface of the heavily deformed **a** A_1 and **b** A_2 regions of the T-SPT sample. **c, d** EBSD analysis showing **c** IPF∥ND map, and **d** map of band contrast superimposed with GBs. In **b**, partial cracks are pointed by yellow arrows; one is magnified and presented in (**b**). In **d**, white, red, and black lines designate LAGBs, MAGBs, and HAGBs, respectively. The yellow arrows in (**c**) point to paired grains on both sides of the crack. The reader is referred to the web version of this paper for the color representation of this figure.

Figure 9 a, b Cross-section view of the fracture surface of the heavily deformed A region of the L-SPT sample. Yellow arrows point to the partial cracks.
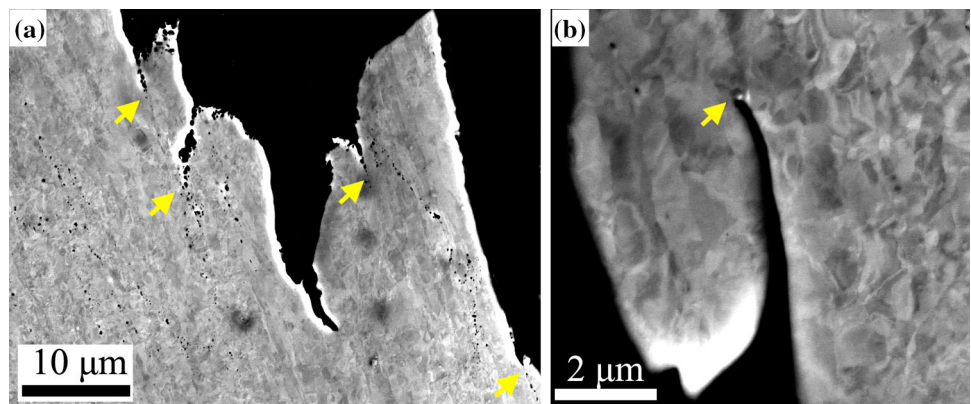
fracture mechanism (Fig. 7e, f). Along the ED, the L sample presented a crack that travels in the plane along two distinct orthogonal vectors (Fig. 7f).

It should be noted that the position of the crack's intersection in the T samples is relatively close to the position where a crack was initiated in the L sample. This issue will be addressed in the discussion section of this manuscript.

Microstructure and texture modification following SPT

Transverse orientation

The cross section of the T-SPT sample included two macro-cracks, the first (A_1) was located closer to the punch center and the second (A_2), closer to clamp, see the explanation of these notations in Fig. 2a. The dominant crack (positioned at the 'A_1' region) propagated through the thickness until a complete
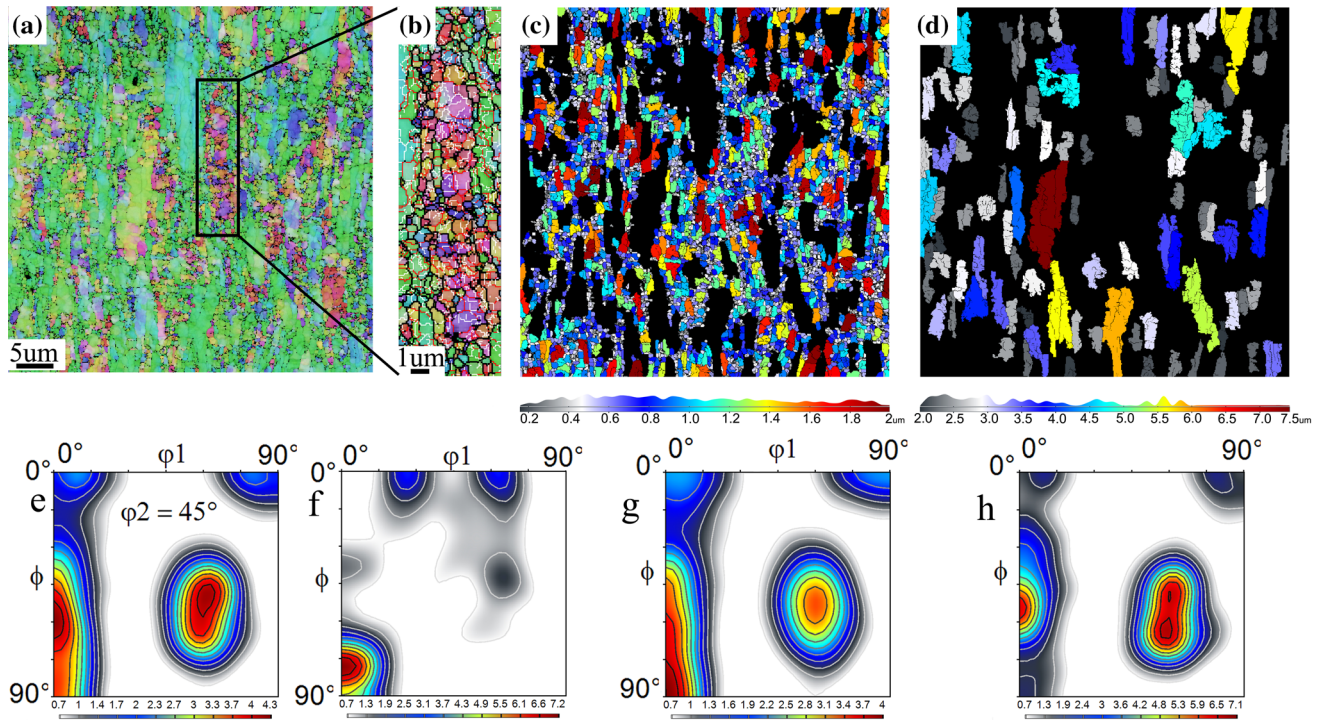
Figure 10 EBSD analysis of the *L*-SPT sample, showing **a** IPF‖ED map, and in **b** a close-up of a region from (**a**) showing fragmented sub-grains. **c** and **d** are grains-structure maps of fine and coarse grains size, respectively; (**e–h**) ODF sections at $\varphi_2 = 45°$, calculated from regions (**a–d**). The grain size histogram is located at the bottom of (**c**) and (**d**). The reader is referred to the web version of this paper for the color representation of this figure.

separation. At the cross section of this zone, the outline of the crack presents a 'zig-zag' pattern with sharp edges originated by secondary cracks (see Fig. 8a). Their length is similar to the distance between closely dispersed particles [21]. The cross section of the A_2 zone, see Fig. 8b, included partial cracks with serrated edges, tilted towards the LD. A close-up of a partial crack is presented on the right corner of Fig. 8b. Several particles were found along the crack path, pointed by yellow arrows in Fig. 8b. In this context, it is possible to assume that these particles act as sequential nodes for crack propagation. This region was further investigated using EBSD. The IPF along the ND (Fig. 8c) was included to better visualize local changes in texture. The IPF‖ND displayed grains with color variations, implying a local misorientation of highly strained grains. The high strain is also manifested by the complex layout of densely packed LAGBs and MAGBs, as seen in the band contrast map in Fig. 8d. Both sides of the micro-crack presented grains with a similar color; some are pointed by yellow arrows (see Fig. 8c). Their relative position and orientation (designated by their color) point to transgranular fracture

propagated through the grains and along with dispersed particles.

Longitudinal orientation

The cross section of the heavily deformed region ('A' zone, Fig. 2b) is presented in Fig. 9a, b. Several cracks are noticed (pointed by yellow arrows in Fig. 9), their edges are blunt, and they are stretched towards the loading axis, which is parallel to the long axis of the elongated grains. Careful examination allowed concluding that fragmented parts of each crack are linked by particles that, as mentioned before, are laced along the grain boundaries (see Fig. 3).

This region was further investigated using EBSD. Following the SP experiment, the grain size distribution of the longitudinal specimen changed, exhibiting a smaller grain size and higher frequency of fine grains. A segmented region of Fig. 10a is magnified in Fig. 10b, presenting elongated packs of fine equiaxed grains surrounded by large elongated grains. The fine grains are bounded by HAGBs, emphasized by black lines. Their intra-grain structure includes cells bounded by LAGBs and MAGBs,

decorated by white and red lines, respectively. To gain a quantitative assessment of the grain distribution, "grain-structure maps" [27] were calculated using the grain-reconstruction method [28], see Fig. 10c, d. The grain size histogram is located at the bottom of each relevant map. The fine grains, defined by smaller than 2.5 µm size, occupy 70% of the investigated surface whereas, at the initial state, grains with similar size fill no more than 50% of the investigated surface.

The complete and segmented EBSD data, shown in Fig. 10a–d, were used to calculate ODFs, and sections at $\varphi_2 = 45°$ are presented in Fig. 10e–h, respectively. Distinct textural differences along the α-fiber were noted. The integrated micro-texture (Fig. 10a) was associated mainly with a strong TG texture component (0°, 54.7°, 45°), throughout the ED direction, up to the RG texture component (0°, 90°, 45°). For the coarsest grains in the deformed structure (seen in Fig. 10d), the micro-texture along the α-fiber was solely linked to the TG texture component, as presented in Fig. 10h. The TG component was also dominant in the fine-sized grains seen in Fig. 10c, yet the RG component was the most intense textural component. In the fine equiaxed grains of Fig. 10b, the micro-texture along the α-fiber was solely related to an intense RG texture component.

Discussion

Correlation between macro deformation mechanisms and mechanical behavior

The main crack initiated at the bottom surface in both L and T orientated specimens, at a closely related peripheral position. At this position, plastic (tensile) stress concentrations result in severe necking, as reported in [29]. Due to the continuous motion of the punch, the crack propagated through the thickness until complete separation.

The different fracture pattern, a ring-shaped for the L sample and facet-shaped for the T sample, is attributed to a different crack path. In the T sample, the crack progressed initially in two directions: the main direction—along the fibrous axis of the grains, which is perpendicular to the LD, and perpendicular to the fibrous axis in which the secondary crack was arrested probably because of the high energy required for its progress. The latter is indicated by a step pattern observed throughout the specimen thickness. The circular-shaped fracture pattern observed in the L sample is commonly associated with ductile and isotropic materials. For this orientation, the crack follows a circumferential path along a localized plastic band in the deformation region. The crack progress by intergranular fracture along the fibrous axis of the grains, which are parallel to the loading direction. Sometimes the crack also crosses grains, as indicated by ductile features in the fracture surface, such as dimples and microvoids.

In the current research, crack nucleation and subsequent propagation were traced to the preferential location of inclusions and carbides (i.e., particles), most of which were found aligned along the ED, decorating the grain boundaries at the pristine state (as-extruded). Their weak cohesive forces between grains and distinct layout might introduce a sequential initiation of localized cleavages at preferential locations yielding constrained induced stress, which imposes preferred sites for crack nucleation and propagation [30, 31].

Aside from stress-motivated crack nucleation, the fracture might also be governed by the local crystallographic texture. The preferential α-fiber texture in the pristine material fulfills conditions for easy cleavage by weak interfaces along the {100} planes, as referred in [32, 33]. Their accounted position, 45° from the ED (see Figs. 7, 8), may explain the observation in current research of the unique 'zig-zag' pattern of crack propagation, as discussed in [34–36].

Correlation between micro deformation mechanisms and mechanical behavior

Although both specimens share the α-fiber texture, current research revealed significant variations in texture components. Especially, differences were visible around the RC component, associated

Table 2 Fraction of different grain boundary types, in [%]

Boundaries type	'L' oriented	'T' oriented
LAGBs	7.2	0.3
MAGBs	16.2	4.2
HAGBs	76.6	95.5
(LAGBs + MAGBs)/HAGBs	30.5	4.7

with crack nucleation and propagation [31], and the TC$_2$ component, known to be the principal component responsible for a significant anisotropy in mechanical properties [37, 38]. The combined effect of these deleterious texture components might suggest that the longitudinally oriented sample is severely prone to failure. On the other hand, it is known that the crack propagation rate is strongly linked to the grain boundary (GB) characteristics, as the GB represents the path for the crack tip propagation. Table 2 summarizes the results of misorientation angle analysis, which was carried out using the EBSD maps (presented in Fig. 4). A higher fraction of MAGBs and LAGBs in the longitudinal section points to the higher activity of dislocations, either entanglement or arrangement as dislocations walls. Both mechanisms act as obstacles to cleavage and, thus, will radically decay crack from propagating on its original path. These findings are in line with the parabolic behavior observed in zone IV at the SP load–displacement curve for the longitudinally oriented sample and the observation of crack blunting in the fracture cross section. For the transverse orientation, cleavage is less hindered by dislocation activity, as can be inferred from Table 2. Nevertheless, the deleterious texture components do not specifically govern this orientation. Thus, the strain flow should be relatively constant, as indicated by the high degree of linearity at the membrane stretching region, in the load–displacement SP curves for the transverse orientation.

Considering the mechanisms derived here, the changes in the microstructure and texture post SPT of longitudinal samples can be understood as a 'sequence of events' that enabled the reduction in thickness during the SP experiments while sustaining the integrity of the materials. The grain boundaries along the ED are plausibly pinned by nano-oxides preventing their movement. This leads to the accumulation of strain within the grain, which eventually leads to fragmentation of the grain. In this way, the originally elongated grains deform through primary fragmentation caused by high dislocation activity. This step is associated with texture transformation from the lowest volumetric stored energy texture components of the RC + TC$_2$ (associated with the pristine state) [39], to a higher volumetric stored energy texture component (TG), for the coarsest grains in the deformed structure (see Fig. 10h). At localized stress regimes, further accommodation of plastic deformation was achieved through secondary fragmentation by cell rotations to the highest volumetric stored energy texture component (RG) until the formation of sub-grains, bounded by high tilt boundaries (see Fig. 10b, g).

The tendency of grains to form those texture components that can absorb higher plastic energy can now be understood as a micro-coping mechanism for plastic deformation. It can be concluded from the analysis performed in current research that for the longitudinal orientation, the local plastic deformation anisotropy is introduced by texture heterogeneity. In the sense of mechanical behavior, this finding is critical as texture heterogeneity reflects on the plastic flow between the neighboring grains since some grains experience greater deformation than their surroundings. It is, therefore, likely that micro-cracks will nucleate at the interfaces between low and high stored energy grains resultant of different ratio of the total amount of slip activity to the von Mises equivalent strain increment [40]. As explained previously, once these cracks initiate, they will propagate along the HAGBs.

At the transverse orientation, the mechanism appears to be somewhat different. At the first glimpse, particles were found along the fracture path, acting as sequential nodes for crack propagation. A thorough examination of the crack pointed at a small angular deviation of the adjacent grains, proving that the crack propagation through the grains has occurred in this case (i.e., transgranular cracking) which is typical to the primary mode of brittle fracture mode. This fracture mechanism differs from that associated with the longitudinal sample since, in the current case, the fracture progressed through the grains and along a path paved by closely dispersed particles.

Conclusions

This study combines small punch testing with advanced characterization techniques to understand the mechanical behavior of 14wt%Cr oxide dispersion steel rod. Specific emphasis was given to the role of anisotropy on the local deformation mechanisms. The main conclusions of the current study are summarized below:

- The as-received state is characterized by elongated grains along the extrusion direction and equiaxed fine-sized grains in the transverse

orientation. A preferential α-fiber texture along the ED was noted for both orientations with significant variations in texture components.

- SPT along the longitudinal and transverse orientations presented anisotropy in mechanical behavior as reflected mainly by the measured deflection.
- The primary mode of fracture in the longitudinal orientation is intergranular ductile along the fibrous axis of the grains, and in the transverse orientation, the fracture occurs in a transgranular brittle mode.
- Accommodation of plastic deformation in the longitudinally oriented specimen is attributed to a micro-coping mechanism, which includes extensive fragmentation of the elongated grains through a complex interplay of dislocations alongside texture modification to components of higher stored energy.
- In the transverse orientation, particles acted as sequential nodes for crack propagation, causing the crack to progress along a path paved by closely dispersed particles.

Acknowledgements

Declarations

Conflict of interest The authors declare that they have no known competing financial interests or personal relationships that could have appeared to influence the work reported in this paper.

References

[1] Kohyama A, Seki M, Abe K, Muroga T, Matsui H, Jitsukawa S, Matsuda S (2000) Interactions between fusion materials R&D and other technologies. J Nucl Mater 283–287:20–27. https://doi.org/10.1016/S0022-3115(00)00156-2

[2] Odette GR, Alinger MJ, Wirth BD (2008) Recent developments in irradiation-resistant steels. Annu Rev Mater Res 38:471–503. https://doi.org/10.1146/annurev.matsci.38.060407.130315

[3] Capdevila C, Bhadeshia HKDH (2001) Manufacturing and microstructural evolution of mechanuically alloyed oxide dispersion strengthened superalloys. Adv Eng Mater 3:647–656. https://doi.org/10.1002/1527-2648(200109)3:9%3c647::AID-ADEM647%3e3.0.CO;2-4

[4] Kimura A, Kayano H, Misawa T, Matsui H (1994) Designation of alloy composition of reduced-activation martensitic steel. J Nucl Mater 212–215:690–694. https://doi.org/10.1016/0022-3115(94)90146-5

[5] Yvon P, Carré F (2009) Structural materials challenges for advanced reactor systems. J Nucl Mater 385:217–222. https://doi.org/10.1016/j.jnucmat.2008.11.026

[6] Fleetwood MJ (1986) Mechanical alloying – the development of strong alloys. Mater Sci Technol 2:1176–1182. https://doi.org/10.1179/mst.1986.2.12.1176

[7] Okada H, Ukai S, Inoue M (1996) Effects of grain morphology and texture on high temperature deformation in oxide dispersion strengthened ferritic steels. J Nucl Sci Technol 33:936–943. https://doi.org/10.1080/18811248.1996.9732035

[8] Rouffié AL, Crépin J, Sennour M, Tanguy B, Pineau A, Hamon D, Wident P, Vincent S, Garat V, Fournier B (2014) Effect of the thermal ageing on the tensile and impact properties of a 18%Cr ODS ferritic steel. J Nucl Mater 445:37–42. https://doi.org/10.1016/j.jnucmat.2013.10.030

[9] de Carlan Y, Bechade J-L, Dubuisson P, Seran J-L, Billot P, Bougault A, Cozzika T, Doriot S, Hamon D, Henry J, Ratti M, Lochet N, Nunes D, Olier P, Leblond T, Mathon MH (2009) CEA developments of new ferritic ODS alloys for nuclear applications. J Nucl Mater 386–388:430–432. https://doi.org/10.1016/j.jnucmat.2008.12.156

[10] Kasada R, Lee SG, Isselin J, Lee JH, Omura T, Kimura A, Okuda T, Inoue M, Ukai S, Ohnuki S, Fujisawa T, Abe F (2011) Anisotropy in tensile and ductile–brittle transition behavior of ODS ferritic steels. J Nucl Mater 417:180–184. https://doi.org/10.1016/j.jnucmat.2010.12.069

[11] Hoelzer DT, Unocic KA, Sokolov MA, Byun TS (2016) Influence of processing on the microstructure and mechanical properties of 14YWT. J Nucl Mater 471:251–265. https://doi.org/10.1016/j.jnucmat.2015.12.011

[12] Gao R, Zhang T, Ding HL, Jiang Y, Wang XP, Fang QF, Liu CS (2015) Annealing effects on the microstructure and mechanical properties of hot-rolled 14Cr-ODS steel. J Nucl Mater 465:268–279. https://doi.org/10.1016/j.jnucmat.2015.05.038

[13] Sahu JK, Krupp U, Ghosh RN, Christ H-J (2009) Effect of 475 °C embrittlement on the mechanical properties of duplex stainless steel. Mater Sci Eng A 508:1–14. https://doi.org/10.1016/j.msea.2009.01.039

[14] Grobner PJ (1972) The 885oF (475 °C) embrittlement of ferritic stainless steels. Metall Trans 4:251–260

[15] Kobayashi S, Takasugi T (2010) Mapping of 475 °C embrittlement in ferritic Fe–Cr–Al alloys. Scripta Mater 63:1104–1107. https://doi.org/10.1016/j.scriptamat.2010.08.015

[16] García TE, Rodríguez C, Belzunce FJ, Suárez C (2014) Estimation of the mechanical properties of metallic materials by means of the small punch test. J Alloy Compd 582:708–717. https://doi.org/10.1016/j.jallcom.2013.08.009

[17] Byun TS, Lee EH, Hunn JD, Farrell K, Mansur LK (2001) Characterization of plastic deformation in a disk bend test. J Nucl Mater 294:256–266. https://doi.org/10.1016/S0022-3115(01)00484-6

[18] Lucas GE (1990) Review of small specimen test techniques for irradiation testing. MTA 21:1105–1119. https://doi.org/10.1007/BF02656531

[19] Fleury E, Ha JS (1998) Small punch tests on steels for steam power plant (II). KSME Int J 12:827. https://doi.org/10.1007/BF02945550

[20] Turba K, Hurst RC, Hähner P (2012) Anisotropic mechanical properties of the MA956 ODS steel characterized by the small punch testing technique. J Nucl Mater 428:76–81. https://doi.org/10.1016/j.jnucmat.2011.08.042

[21] Templeman Y, Rogozhkin S, Khomich A, Nikitin A, Pinkas M, Meshi L (2020) Characterization of nano-sized particles in 14%Cr oxide dispersion strengthened (ODS) steel using classical and frontier microscopy methods. Mater Charact 160:110075. https://doi.org/10.1016/j.matchar.2019.110075

[22] Haroush S, Priel E, Moreno D, Busiba A, Silverman I, Turgeman A, Shneck R, Gelbstein Y (2015) Evaluation of the mechanical properties of SS-316L thin foils by small punch testing and finite element analysis. Mater Des 83:75–84. https://doi.org/10.1016/j.matdes.2015.05.049

[23] Haroush S, Moreno D, Silverman I, Turgeman A, Shneck R, Gelbstein Y (2017) The mechanical behavior of HAVAR foils using the small punch technique. Materials 10:491. https://doi.org/10.3390/ma10050491

[24] Cwa C (2006) cwa200615627 - 15627 workshop agreement: small punch test method for metallic materials. European Committee for Standardization, Brussels

[25] Beausir B, Fundenberger J-J (2017) Analysis tools for electron and X-ray diffraction, ATEX - software. http://www.atex-software.eu/help.html (Accessed 17 July 2021)

[26] Brandon DG (1966) The structure of high-angle grain boundaries. Acta Metall 14:1479–1484. https://doi.org/10.1016/0001-6160(66)90168-4

[27] Samuha S, Kahana E, Sadot O, Shneck R (2018) Improved formability of Mg-AZ80 alloy under a high strain rate in expanding-ring experiments. Materials 11:329. https://doi.org/10.3390/ma11020329

[28] Humphreys FJ (2004) Reconstruction of grains and subgrains from electron backscatter diffraction maps: reconstruction of grains and subgrains from EBSD maps. J Microsc 213:247–256. https://doi.org/10.1111/j.0022-2720.2004.01297.x

[29] Hähner P, Soyarslan C, Gülçimen Çakan B, Bargmann S (2019) Determining tensile yield stresses from small punch tests: a numerical-based scheme. Mater Des 182:107974. https://doi.org/10.1016/j.matdes.2019.107974

[30] Yen CM, Stickels CA (1970) Lamellate fracture in 5150 steel processed by modified ausforming. Metall Mater Trans B 1:3037–3047. https://doi.org/10.1007/BF03038417

[31] Zhou W, Loh NL (1996) Effect of delaminations on improvement of notch toughness at low temperatures. Scripta Mater 34:633–639. https://doi.org/10.1016/1359-6462(95)00564-1

[32] Yerra SK, Tekog-Lu C, Scheyvaerts F, Delannay L, Van Houtte P, Pardoen T (2010) Void growth and coalescence in single crystals. Int J Solids Struct 47:1016–1029. https://doi.org/10.1016/j.ijsolstr.2009.12.019

[33] Ray RK, Jonas JJ (1990) Transformation textures in steels. Int Mater Rev 35:1–36. https://doi.org/10.1179/095066090790324046

[34] Bourell DL, Sherby OD (1983) Texture induced cleavage delamination of warm-rolled low carbon steel. Metall Mater Trans A 14:2563–2566. https://doi.org/10.1007/BF02668900

[35] Inoue T, Kimura Y, Ochiai S (2011) Static fracture toughness of fail-safe steel. Scripta Mater 65:552–555. https://doi.org/10.1016/j.scriptamat.2011.06.025

[36] García-Junceda A, Hernández-Mayoral M, Serrano M (2012) Influence of the microstructure on the tensile and impact properties of a 14Cr ODS steel bar. Mater Sci Eng A 556:696–703. https://doi.org/10.1016/j.msea.2012.07.051

[37] Okaguchi S, Makino H, Hamada M, Yamamoto A, Ikeda T, Takeuchi I, Fairchild DP, Macia ML, Papka SD, Stevens JH, Petersen CW, Koo JY, Bangaru NV, Luton MJ (2003) Development and mechanical properties of X120 linepipe. In: Proceedings of The Thirteenth (2003) International Offshore and Polar Engineering Conference Honolulu, Hawaii, USA, May 25–30

[38] Koo JY, Luton MJ, Bangaru NV, Petkovic RA, Fairchild DP, Petersen CW, Asahi H, Hara T, Terada Y, Sugiyama M, Tamehiro H, Komizo Y, Okaguchi S, Hamada M, Yamamoto A, Takeuchi I (2004) Metallurgical design of ultra high-strength steels for gas pipelines. Int J Offshore Polar Eng 14:1

[39] Hutchinson B (1999) Deformation microstructures and textures in steels, philosophical transactions of the royal society of London. Ser A Math Phys Eng Sci 357:1471–1485. https://doi.org/10.1098/rsta.1999.0385

[40] Haskel HL, Pauletti E, de Martins JP, de Carvalho ALM (2014) Microstructure and microtexture assessment of delamination phenomena in charpy impact tested specimens. Mat Res 17:1238–1250. https://doi.org/10.1590/1516-1439.268314